The Effect of Metalloprotein Inhibitors on Cellular Metal Ion Content and Distribution

Yao Chen[a,b], **Barry Lai**[c], **Zhenjie Zhang**[a,b], and **Seth M. Cohen**[b]

[a]State Key Laboratory of Medicinal Chemical Biology, Nankai University, Tianjin, 300350, China

[b]Department of Chemistry and Biochemistry, University of California, San Diego, La Jolla, California 92093, USA

[c]X-ray Science Division, Advanced Photon Source, Argonne National Laboratory, Argonne, IL 60439, USA

Abstract

With metalloproteins garnering increased interest as therapeutic targets, designing target-specific metalloprotein inhibitors (MPi) is of substantial importance. However, in many respects, the development and evaluation of MPi lags behind that of conventional small molecule therapeutics. Core concerns around MPi, such as target selectivity and potential disruption of metal ion homeostasis linger. Herein, we used a suite of analytical methods, including energy-dispersive X-ray spectroscopy (EDX), inductively coupled plasma atomic emission spectroscopy (ICP-OES), and synchrotron X-ray fluorescence microscopy (SXRF) to investigate the effect of several MPi on cellular metal ion distribution and homeostasis. The results reveal that at therapeutically relevant concentrations, the tested MPi have no significant effects on cellular metal ion content or distribution. In addition, the affinity of the metal-binding pharmacophore (MBP) utilized by the MPi does not have a substantial influence on the effect of the MPi on cellular metal distribution. These studies provide an important, original data set indicating that metal ion homeostasis is not notably perturbed by MPi, which should encourage the development of and aid in designing new MPi, guide MBP selection, and clarify the effect of MPi on the 'metallome'.

Graphical Abstract
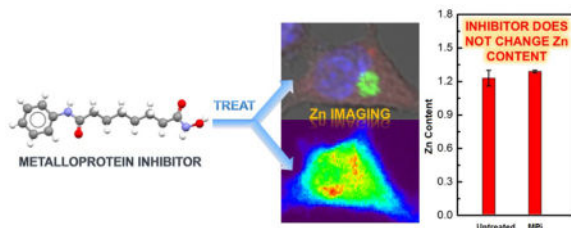
Introduction

Metal cations are indispensable components of the cellular machinery and are involved in numerous tasks ranging from nucleic acid and protein structure stabilization to enzymatic catalysis, signal transduction, muscle contraction, hormone secretion, taste and pain sensation, respiration, and photosynthesis (1–4). Therefore, unsurprisingly, metal ion

homeostasis plays a critical role in many biological processes and disease states (5, 6). It is well known that transition metal ions play a major role in the dynamic processes of disease. For example, intracellular free Cu must be strictly limited as the uncontrolled accumulation of Cu may lead to increased oxidative stress and damage to macromolecules (7–9). Similarly, metalloproteins are essential to numerous biological processes and represent a broad class of validated clinical targets (10, 11). Metalloprotein inhibitors (MPi) are generally comprised of a metal-binding pharmacophore (MBP) and 'backbone' substituents (12). MPi are used to treat a variety of illnesses including hypertension, cancer, and infectious diseases, thereby have a significant impact on improving human health (12, 13). However, despite their importance, MPi are underdeveloped compared to conventional small molecule therapeutics. Although ~33% of all proteins are metalloproteins, there are only ~20 FDA-approved MPi (excluding cytochrome-targeting antifungals) (14). Indeed, a lack of studies into the binding mode, affinity, selectivity, and pharmacological behavior of MPi has slowed efforts to develop this important class of therapeutics. Apprehensions remain regarding the use of MPi due to concerns over inhibitor selectivity (e.g. off-target effects), as well as effects on metal ion trafficking and homeostasis. Although these concerns are frequently raised, few studies have directly evaluated these issues (15–17). We have recently evaluated the selectivity of several MPi against their target metalloproteins and demonstrated that a variety of MPi do not show off-target activity, even at concentrations far above those required to completely inhibit their targets. In addition, we have demonstrated that in the presence of competing metalloproteins the activity of MPi for their targets is not muted (15, 18). With respect to effects on metal ion homeostasis, in vitro experiments suggest that MPi are not capable of removing iron from transferrin (15), which is a major pathway for metal ion homeostasis and distribution and a source of iron for pathogenic bacteria via the action of siderophores (19). To accrue key information critical for designing MPi and understanding the effects of MPi on the 'metallome', a more comprehensive evaluation of MPi, specifically the effects of MPi on metal ion distribution at the cellular and sub-cellular level is required.

Our previous enzyme-based studies showed that MPi present excellent selectivity and specificity for their targets, which encouraged us to further examine the effect of MPi on metal ions in whole cells, and directly evaluate effects on cellular metal ion homeostasis. Recently, some advanced molecular probes have been developed for the detection of cellular transition metals (20, 21). However, for multi-element mapping and the detection of trace metals with very low cellular content, some challenges remain. With submicron spatial resolution for multi-element mapping, synchrotron X-ray fluorescence microscopy (SXRF) provides an excellent method for tracking cellular metal ion distribution (22–24). SXRF can distinguish between metal ions such as Fe, Ni, Cu, and Zn within an individual cell in a single experiment and has been used to evaluate metal concentrations and distributions in numerous studies using various cell types (25–30). To the best of our knowledge, SXRF has not been utilized to examine the effect of an MPi (or any enzyme inhibitor) on the distribution of metal ions in cells. In scanning electron microscopy (SEM), backscattered electron images display compositional contrast that comes from different elements and their distribution. Energy dispersive X-ray spectroscopy (EDX) can identify those particular elements and their relative proportions. Inductively coupled plasma atomic emission

spectroscopy (ICP-OES) can be used to measure overall cellular metal content. Herein, all of these techniques were used to study NIH3T3 mouse embryonic fibroblast cells as a model system for the effects of MPi on cellular metal ion content and distribution (31). Fibroblast cell lines are well known to be suitable for in vitro studies of cell change/damage due to various external factors. NIH3T3 are adherent cells that can be cultured in low density allowing easy visual inspection and sample preparation (26, 27, 32).

The effect of MPi on cellular metal ion homeostasis, primarily Zn and Cu, was investigated by evaluation of the changes in: a) the total metal ion content of cells, and b) the distribution of metal ions in sub-cellular level. In addition, we also investigated whether the influence of MPi on metal homeostasis was dependent on the metal-binding affinity of the MPi. MPi were employed that share a common Zn-metalloprotein target, histonedeacetylases (HDACs); however, these MPi utilize different metal-binding pharmacophores (MBPs) that possess a range of metal ion affinities. These MPi were selected to determine whether any changes in metal ion distribution were correlated with the metal affinity of the MBP. Cells were treated with one of three HDAC inhibitors (HDACi, Fig. 1): a) SAHA (suberoylanilide-hydroxamic acid, Vorinostat) (33), an FDA-approved HDACi containing the high affinity hydroxamic acid MBP; b) entinostat (MS-275) (34), an HDACi in clinical trials that has a weaker benzamide-based MBP and is characterized by slow rates of binding (35); and c) TFMO-1, (*N*-{[4-(4-phenyl-1,3-thiazol-2-yl)oxan-4-yl]methyl}-3-[5-(trifluoromethyl)-1,2,4-oxadiazol-3-yl]benzamide), a recently reported HDACi that is based on a trifluoromethyloxadiazole MBP warhead that has little metal-binding affinity (36). By analyzing the crystal structure of these MPi, Nolan *et al.* reported that TMFO-1 interacts with the catalytic Zn(II) at the distance of ~3.0 Å, while the typical Zn bond distance of the hydroxamate and benzamide inhibitors (e.g. SAHA and Entinostat) is ~2.0 Å (36), indicating the different Zn-binding affinity of the selected MPi. Our hypothesis was that if the inhibitors showed different effects on metal ion distribution and homeostasis, then this might be correlated to differences in MBP affinity (33–36). However, if all three inhibitors generated similar results, this would indicate that effects on metal ion distribution (which could also include no effects) are simply part of a common cellular response to on-target HDAC inhibition and not correlated specifically with metal-binding ability. In addition to these HDACi, the strong metal chelator TPEN (*N,N,N′,N′*-tetrakis (2-pyridylmethyl)ethane-1,2-diamine) was used as a control compound for metal removal in this study (Fig. 1). TPEN has a much higher metal binding affinity than SAHA or entinostat (29, 30) and only moderate cytotoxicity ($EC_{50} = 26$ μM). As a control for metal ion uptake, cells were treated with $ZnCl_2$ in the presence of pyrithione, the latter of which is a known ionophore that facilitates the cellular uptake of Zn(II) (6).

Results and Discussion

Determination of Sub-lethal MPi Concentrations

The EC_{50} of each compound against NIH3T3 was tested, so that sub-lethal concentrations of MPi would be used in subsequent studies based on their EC_{50} and IC_{50} values. Cytotoxicity assays of SAHA, entinostat, TFMO-1, and TPEN (Fig. 1) were conducted with the NIH3T3 cell line (Fig. S1). The results listed in Table 1 indicate low cytotoxicity for TFMO-1 (EC_{50}

= 75 μM) and entinostat (EC_{50} = 41 μM). However, SAHA demonstrated relative high cytotoxicity (EC_{50} = 5 μM) against the NIH3T3 cell line. Due to the differences in MPi cytotoxicity, different concentrations of MPi were used to treat the cells. The selected concentrations for each MPi are close to the EC_{80} values of the compounds, allowing for cell growth, while maximally challenging the cell to exhibit changes in cellular metal homeostasis. Sub-lethal concentrations of MPi, which are higher than the reported IC_{50} values against HDACs (e.g. the IC_{50} values of SAHA against HDAC-1, -2, and -6 are 53 nM, 10 nM, and 22 nM, respectively) (15, 18, 28), and significantly lower than the EC_{50} were used to evaluate the effect of MPi on cellular metal ion distribution (Table 1), so that the selected concentrations of MPi are high enough to inhibit HDACs without resulting in acute cytotoxicity.

Whole Cell Metal Content by ICP-OES

ICP-OES was used to measure the whole cell metal content and determine if there was a substantial change in extracellular metal concentrations (i.e. large efflux or influx from the cell) after the treatment with HDACi (SAHA, entinostat, TMFO-1) or the control compounds (TPEN, $ZnCl_2$/pyrithione). NIH3T3 cells were treated with one of the following (Table 1): 1.7 μM SAHA, 5.1 μM entinostat, 5.1 μM TMFO-1, 1.7 μM TPEN, or 1.7 μM $ZnCl_2$/0.28 μM pyrithione, with untreated NIH3T3 cells as a baseline control. Three independent samples for each treatment condition were analyzed by ICP-OES. To normalize the ICP-OES results, the ICP-OES data for each experiment was normalized by the mass of protein in the sample (Fig. 2). The protein content for each sample was determined following the protocol of an improved Bradford protein assay (34). As expected, the $ZnCl_2$/ pyrithione treated cells contained significantly greater amounts of Zn when compared to untreated cells, which is due to the ionophore pyrithione that chaperones Zn into the cells. Interestingly, in $ZnCl_2$/pyrithione treated cells, a greater Cu and Fe content was also observed (Table S1, S2), which may also be due to the pyrithione ionophore facilitating the uptake of these metal ions from the medium (6). The 3.4 and 5.1 μM TPEN treated samples exhibited a slight decrease in Zn content. SAHA, entinostat, and TMFO-1 treated cells showed Zn levels comparable to the untreated controls. It is noteworthy that the concentrations of HDACi used in these experiments is much higher than the IC_{50} of these compounds for their target metalloprotein; therefore, the ICP-OES data demonstrates that exposure to sub-lethal concentrations of HDACi exhibit no perturbation on the overall cellular metal content. ICP-OES is a bulk measurement of total cellular metal content, and hence experiments to examine metal ion changes at the sub-cellular level were pursued.

SEM-EDX

In order to evaluate the effect of MPi on cellular metal ion homeostasis, the metal distribution in NIH3T3 cells upon the exposure to MPi/controls was determined. UHR (Ultra High Resolution) SEM can capture the cell biofilm images with high resolution (Fig. S2) and EDX can quantitatively analyze the relative content of elements, as well as qualitatively map the elemental distribution in samples (Fig. S3). SEM-EDX was used to detect changes in cellular Zn distribution, providing the relative Zn abundance (shown as % abundance of Zn among the overall content of the tested elements). Phosphorus was used as a reference element due to its relative constant concentration in cells, with data reported as a

Zn/P molar ratio (Fig. 3, Table S3)(37). Cells were treated with sub-lethal concentrations of each compound (Table 1) and the data is summarized in Fig. 3. Cells treated with the HDACi – SAHA, entinostat, and TMFO-1 – contained comparable amount of Zn as untreated cells. Importantly, TPEN treated samples demonstrated a concentration dependent decrease of cellular Zn content, while $ZnCl_2$/pyrithione treated cells contain more Zn than untreated cells. The pattern shown in the quantitative EDX study are consistent with that observed in the ICP-OES test. Unfortunately, due to the detection limit of EDX, we were only able to test the most abundant metal (Zn) and could not detect metals with lower cellular abundance (e.g. Cu, Fe, Co, Ni, Co). In addition to this quantitative analysis of cellular Zn amount, qualitative mapping of cellular Zn distribution was also conducted on SAHA treated samples. The Zn distribution in SAHA treated cells resembles that of untreated cell (Fig. S3), suggesting little or no alteration of cellular Zn trafficking.

Confocal laser scanning microscopy (CLSM) and SXRF

To quantitatively observe changes in intracellular metal distribution, correlation of cellular metal mapping with the sub-cellular structure was performed. SXRF (Beamline 2-ID-D) correlated with confocal laser scanning microscopy (CLSM) was used to track the changes in cellular metal ion distribution upon exposure to HDACi. Cells were initially imaged by CLSM to locate sub-cellular structures (e.g. Golgi body, mitochondria, nucleus) and then the cellular metal ion distribution of the same cells was mapped by SXRF. By overlaying the confocal image and the SXRF mapping, the distribution of metal ions in sub-cellular level was determined.

Establishing a good sample preparation protocol is critical for SXRF. The challenges in sample preparation rely largely on three factors: the growth of NIH3T3 cells on silicon nitride windows (Silson), organelle staining, and the alignment of CLSM cell images with SXRF maps. Generally, NIH3T3 cells do not grow on bare silicon nitride windows. Therefore, the silicon nitride windows are coated to facilitate cellular growth. Three coating agents were tested: 0.1% poly L-lysine(Sigma), gelatin gel (Sigma), and human fibronectin (Corning). Fibronectin demonstrated the best coating performance and lead to fast and stable growth of NIH3T3 cells on the silicon nitride surface.

After a series of attempts with different staining agents and various conditions, organelle staining was optimized as follows: MitoTracker-Red FM (red), CellLight GFP (green), and Hoechst 33343 (blue) to stain the mitochondria, Golgi body, and nucleus, respectively (Fig. S4). The cells were fixed to improve the cell stability during confocal imaging (Fig. 4a). At least two samples per HDACi treatment were prepared and imaged before transportation to Argonne National Lab for SXRF mapping. In order to reduce the background noise from sample preparation, the samples were washed twice by 0.1 M ammonium acetate before drying. SXRF mapping indicated that the proper washing can substantially reduce the signal from Cl, avoiding signal interference with important reference elements, such as S.

SXRF microscopy was performed at the 2-ID-D beamline of the Advanced Photon Source located at the Argonne National Laboratory (IL, USA). Cells attached to the silicon nitride windows were placed onto a kinematic specimen holder suitable for both optical and X-ray fluorescence microscopies. The holder was first mounted on a light microscope (Leica

DMXRE) and target cells were located on the grid relative to a pre-determined reference point using a motorized x/y stage. The coordinates of each cell were located under the light microscope, recorded, and then converted to the coordinates of the cells on the microprobe specimen holder for SXRF using a programed table. For SXRF excitation, a monochromatic X-ray beam generated by an undulator source was focused to a spot size of 0.3×0.3 μm^2 on the specimen, and the excitation was set to 10 keV to ensure X-ray emission from all first-row transition elements. The sample was scanned with a step size of 0.3 μm, and the energy dispersive silicon drift detector was used to acquire the X-ray emission spectrum. Elemental maps (Fig. 4b) were generated with the MAPS software package by Gaussian fitting of the raw emission spectra for each image pixel (38). The Gaussian peaks were matched to characteristic X-ray emission lines to determine the fluorescence signal for each element. Considering cell-to-cell variations, in order to gather sufficient statistics to determine the changes in cellular metal ion distribution, at least five cells were scanned for each treatment regimen. After the SXRF data collection, the elemental mapping result of each cell was first matched with its CLSM image (Fig. 4). By overlaying the CLSM image with the cellular elemental map, regions of interest (e.g. nucleus, Golgi body, mitochondria) could be outlined (Fig. 4b) using the MAPS software for further quantitative analysis.

Overall cellular metal content was first assessed. As expected, the $ZnCl_2$/pyrithione treated cells show significantly higher Zn than untreated cells, which confirmed correct calibration of the method. Other metal ions (e.g. Fe, Cu) also increased upon the exposure to $ZnCl_2$/pyrithione, likely because the pyrithione ionophore facilitated the uptake of these metals from the environment. Treatment with a high concentration of TPEN (5.1 μM) led to the decrease of other cellular metal ions (Fe, Ni, Cu, Zn). Surprisingly, the cells treated with low concentration of TPEN (1.7 μM) indicated no significant change of Zn, but a decrease of Cu was observed (Fig. 5). Two HDACi, SAHA and entinostat, were evaluated by SXRF. TMFO-1 has the weakest Zn-binding affinity, so it was not utilized in these experiments due to limited beamtime. SAHA (1.7 μM) treated samples showed unchanged levels of Zn content and other metals of interest (e.g. Fe, Ni, Cu) when compared to untreated cells. The 5.1 μM entinostat treated samples demonstrated a slight decrease in both Zn and Cu, which is probably due to the higher concentration of entinostat (5.1 μM) used in this experiment because of the lower IC_{50} value of the inhibitor (the IC_{50} of entinostat for HDAC-1 is ~ 240 nM) (39). The 1.7 μM entinostat treated sample supported this interpretation, as no decrease of Cu or Zn was observed (Table S1, S4). Overall, the SXRF findings revealed no significant disruption in overall cellular metal content by these HDACi, which is consistent with the ICP-OES and EDX studies.

To investigate possible changes in cellular metal ion distribution upon HDACi exposure, a further analysis of the metal distribution at the sub-cellular level was performed. Confocal images of cells were overlaid with SXRF elemental mapping, and the metal content (Cu, Zn) in Golgi bodies, mitochondria, and nuclei was examined in each sample (Fig. 6).

Treatment of NIH3T3 cells with 1.7 μM Zn/0.28 μM pyrithione leads to an increase of Zn in all three regions of interest (Golgi body, mitochondria, nuclei). A slight increase of Cu is also observed in all three areas, probably due to the uptake of Cu facilitated by the pyrithione ionophore. Surprisingly, after exposure to 1.7 μM TPEN, no change in Zn

distribution was observed in these cells. As expected, at higher TPEN concentrations (5.1 μM) a significant decrease of Zn is observed in all three regions. Both the 1.7 and 5.1 μM TPEN treated samples showed similar decreases in Cu. Importantly, neither of the HDACi (1.7 μM SAHA, 5.1 μM entinostat) showed notable changes in Cu or Zn distribution, even at concentrations far above the IC_{50} values of these inhibitors against their HDAC targets. Overall, the mapping studies simply mirror the overall changes in cellular metal ion content, with no organelle specific changes observed with any of the control compounds or HDACi.

In summary, a suite of analytical methods, including ICP-OES, SEM-EDX, and SXRF were used to investigate the effects of HDACi on cellular metal ion homeostasis. The results revealed these inhibitors do not significantly influence cellular metal ion distribution or homeostasis, even at concentrations far above their IC_{50} values against their target proteins. The findings in this study similarly suggest that the metal binding affinity of MBP in these inhibitors also does not directly influence cellular metal distribution.

Due to detection and resolution limits, ICP-OES and EDX are incapable of tracking nuanced effects on sub-cellular metal distribution. However, they provided valuable information to confirm the SXRF data, and thus the three methods construct a self-consistent picture that support to our conclusions. ICP-OES provides the bulk measurement of total cellular metal content and detected no substantial changes in metal ion concentrations (i.e. large efflux or influx from the cell) upon exposure to HDACi. The most abundant cellular metal (Zn) was also studied by EDX. The results (molar ratio of Zn/P) indicated a higher amount of Zn in $ZnCl_2$/pyrithione-treated sample, and demonstrated a decrease in Zn after the treatment with TPEN. More importantly, EDX provided results consistent with ICP-OES, supporting no significant effects on overall Zn cellular distribution. However, EDX was only suitable to provide qualitative information for cellular metal mapping.

The SXRF results provided the quantitative mapping of multi-elemental distributions at the sub-cellular level, and demonstrated no noteworthy changes the intracellular distribution of important metals (e.g. Cu, Zn) upon exposure to HDACi. To the best of our knowledge, this is the first work that provides direct measurements regarding the effects of HDACi, or any MPi, on cellular metal ion distribution. Our conclusion from these measurements is that MPi have little to no impact on cellular metal distribution and homeostasis under the conditions explored here. We expect these findings will help to resolve and alleviate concerns that are central to designing MPi and to what degree these factors merit consideration in the development of MPi therapeutics.

Materials and Methods

Cell Culture

NIH3T3 cell line was cultivated in DMEM medium supplemented with 10% fetal bovine serum (Gibco, Grand Island, NY, USA) at 37 °C in an incubator with 5% CO_2. In order to protect the cells from contamination, 1% antibiotic (Penicillin Streptomycin) was also added.

General Protocol

All reagents and SAHA, TPEN, entinostat, were purchased from Sigma Aldrich, and TFMO-1 was purchased from MedKoo Biosciences, Inc. Experiments were initially performed on NIH3T3 mouse fibroblasts. Cells were incubated with HDACi and appropriate controls at sub-lethal concentrations, which were based on cytotoxicity studies. After dosing for ~2 h, both treated and untreated cells were evaluated by ICP-OES, EDX, or SXRF for quantitative mapping of any difference in metal ion abundance or distribution between treated and untreated cells. The total metal content was determined by ICP-OES.

Cytotoxicity assay

NIH3T3 cells were cultured to log phase ($1~6 \times 10^6$ cells/mL) and the number of live cells based on cell counting using trypan blue stain. Cells were diluted to the desired concentrations using culture medium, and then plated in the 96-well plates (100 μL per well, ~5000 cells per well for NIH3T3). The cells were cultured overnight in 5% CO_2 atmosphere at 37°C. A series of stock solution of different compounds (HDACi) were made using culture medium. The medium was removed from each well in the 96-well plate. The cells were exposed to compounds by adding 100 μL of various concentrations of compound solution into each well. The assays were performed in triplicate. The negative control wells without added inhibitor were arbitrarily set as 100% viability. The plates were incubated in 37 °C and 5% CO_2 for 70 h. Subsequently, 20 μL of CellTiter 96® AQueous One Solution Reagent was added into each well in the 96-well assay plate. The plates were then incubated for 2h in a humidified atmosphere (5% CO_2) at 37°C. And then record the absorbance at 490 nm using BioTek Synergy HT microplate reader.

ICP-OES

NIH3T3 cells were cultured to 70% confluence and the number of live cells was determined by cell counting. Cells were then diluted to the desired concentration using culture medium, and 1 mL of cell solution was sub-cultured to each cell culture flask (Subcultivation Ratio: inoculate ~5 ×10³ cells/mL). The cells were cultured for ~2 d at 37 °C with 5% CO_2 (reaching ~ 70% confluence), and then treated with MPi or appropriate controls at sub-lethal concentrations (Table 1). Cells in each flask were then separated from the media, and washed once with PBS, and isolated by centrifuging at 10000g for 4 min. The protein content in each collected cell pellet was determined separately using an improved Bradford assay (40). In this assay, the absorbance at 450 and 590 nm were measured and the A590/A450 ratio gave a linear relationship over a wide concentration range. The standard curve was constructed by adding 0–50 μL of bovine serum albumin (BSA, 0.1 mg/mL) in 0.001% Triton X-100 to triplicate wells of a 96-well plate. The total volume of each well was raised to 100 μL by 0.001% Triton X-100. 100 μL of Bradford Reagent was then added to each well. The samples were incubated for 5–60 min for color development and the absorbance at 450 and 590 nm was recorded using BioTek Synergy HT microplate reader to construct the calibration curve. The cell pellet of each sample was digested by adding a certain amount of 0.001% Triton X-100 (usually 3–5 mL depending on the amount of harvested cells). 1 mL of the digested solution was used for the Bradford assay, and the rest solution was lyophilized. These samples containing unknown amount of protein quantified using the Bradford assay.

The lyophilized samples were then digested by adding 100 μL of concentrated nitric acid (Fisher scientific) overnight, heated to 55 °C for 6 h, and then 0.001% Triton X-100 was added followed by heating overnight at 55 °C to complete the digestion. The total content of each metal (Fe, Cu, Zn) was determined by ICP-OES under operating conditions suitable for routine multi-element analysis. The instrument was calibrated using 0, 5, 10, 50, 100, and 500 parts per billion (ppb) of certified multi-element ICP standard calibration solutions (Inorganic Ventures, IV-STOCK-13) prepared in ICP tuning solution (2 wt% HNO_3, with 1 μg/L Ce, Co, Li, Mg, Tl, and Y as internal standards).

SEM-EDX

An image of the sample surface was constructed by measuring secondary electron intensity as a function of the position of the scanning primary electron beam. SEM-EDX allows one to identify different elements and their relative proportions (e.g. Atomic %). To prepare the sample, the NIH3T3 cells were first grown on sterile glass coverslips until 70–80% confluence, and then the cells were treated with MPi or control compounds for 2 h (Table 1). The treated and untreated cells (grown on coverslips) were washed with PBS buffer once, fixed for 10 min, washed with PBS one more time, and dried using ethanol. Dried samples were mounted on a holder for EDX measurements. Samples were transferred to conductive carbon tape on a sample holder disk, and coated by Ir-sputter coating for 8 sec. A FEI SFEG UHR SEM instrument was used for acquiring images under vacuum. The elemental mapping images and the relative proportions of each tested element (e.g. Zn and P) were processed and displayed using the Iridium Ultra software suite, and the data was then normalized using the Zn/P ratio.

Cell staining and CLSM imaging

In order to investigate the cellular metal ion distribution and trafficking, several organelles were stained and imaged using CLSM before SXRF tests. SXRF metal mapping can be aligned with the confocal images to correlate the location of organelles with changes in metal distribution upon the exposure to certain compounds. The Golgi body was stained using CellLight GFP BacMam 2.0; the mitochondria were stained with MitoTracker® Red CMXRos; and the nucleus was stained with Hoechst 33342 (all staining reagents were purchased from ThermoFisher Scientific). All staining was conducted following the standard protocol provided by the manufacturers. CLSM images of the stained samples were taken under 20 × amplification. The location of the imaged cells were carefully marked and recorded in order to be relocated during SXRF.

SXRF

For SXRF measurements, NIH3T3 cells were grown on the surface of silicon nitride windows in TEM grids (membrane thickness: 500 nm, Silson) using the culture conditions mentioned above. The grids were sterilized with ethanol and the silicon nitride windows were coated in human fibronectin (Corning) to facilitate cell growth. The coated windows were placed in the wells of 24-well plates, and 1 mL of pre-warmed complete growth medium was added into each well. The cells were then placed in each well with the optimized subculture ratio (~5×10^4 cells/mL). After overnight growth at 37 °C and 5% CO_2 atmosphere, the Golgi apparatus, mitochondria, and nucleus of the cells were stained (see

CLSM above). The cells were then fixed with pre-warmed 4% paraformaldehyde for 10 min at room temperature, and washed twice with 0.1M ammonium acetate (Sigma-Aldrich) to reduce the possible background for SXRF scanning. Finally, samples were air-dried overnight in a covered, sterile cell culture dish. SXRF microscopy was performed at beamline 2-ID-D of the Advanced Photon Source at the Argonne National Laboratory. Incident X-rays of 10 keV energy were chosen to excite elements from P to Zn. A Fresnel zone plate focused the X-ray beam to a spot size of $0.3 \times 0.3 \ \mu m^2$ on the specimen, which was raster-scanned. XRF from the specimen was captured with an energy dispersive silicon drift detector. Spectral analysis of the fluorescence spectrum of each raster pixel then provided spatial images for each element. The collected data was analyzed and plotted by MAPS software.

Supplementary Material

Refer to Web version on PubMed Central for supplementary material.

Acknowledgments

References

1. Frausto da Silva, JJR. The biological chemistry of the elements: The inorganic chemistry of life. Oxford University Press; Oxford, UK: 1991.

2. Lippard, SJ., Berg, J. Principles of bioinorganic chemistry. University Science Books; Mill Valley, California: 1994.

3. Christianson DWC, JD. Catalysis By Metal-Activated Hydroxide in Zinc and Manganese Metalloenzymes. Annu Rev Biochem. 1996; 68:25.

4. Bertini, I.Sigel, A., Sigel, H., editors. Handbook on Metalloproteins. Marcel Dekker; New York: 2001.

5. Bleackley MR, MacGillivray RTA. Transition metal homeostasis: from yeast to human disease. BioMetals. 2011; 24(5):785–809. [PubMed: 21479832]

6. Colvin RA, Lai B, Holmes WR, Lee D. Understanding metal homeostasis in primary cultured neurons. Studies using single neuron subcellular and quantitative metallomics. Metallomics. 2015; 7(7):1111–1123. [PubMed: 25894020]

7. Wang J, et al. Inhibition of human copper trafficking by a small molecule significantly attenuates cancer cell proliferation. Nat Chem. 2015; 7(12):968–979. [PubMed: 26587712]

8. Jomova K, Valko M. Advances in metal-induced oxidative stress and human disease. Toxicology. 2011; 283(2–3):65–87. [PubMed: 21414382]

9. Barilli A, et al. Oxidative Stress Induced by Copper and Iron Complexes with 8-Hydroxyquinoline Derivatives Causes Paraptotic Death of HeLa Cancer Cells. Mol Pharm. 2014; 11(4):1151–1163. [PubMed: 24592930]

10. Schmitt HM, Schlamp CL, Nickells RW. Role of HDACs in optic nerve damage-induced nuclear atrophy of retinal ganglion cells. Neurosci Lett. 2016; 625:11–15. [PubMed: 26733303]

11. Halim ATA, Ariffin NAFM, Azlan M. Review: the Multiple Roles of Monocytic Microparticles. Inflammation. 2016; 39(4):1277–1284. [PubMed: 27216803]

12. Rouffet M, Cohen SM. Emerging trends in metalloprotein inhibition. Dalton Trans. 2011; 40(14): 3445–3454. [PubMed: 21290034]

13. Yang Y, et al. Metalloprotein Inhibitors for the Treatment of Human Diseases. Curr Top Med Chem. 2016; 16(4):384–396. [PubMed: 26268345]

14. Drug@FDA. 2016. (http://www.accessdata.fda.gov/scripts/cder/drugsatfda/index.cfm)

15. Day JA, Cohen SM. Investigating the Selectivity of Metalloenzyme Inhibitors. J Med Chem. 2013; 56(20):7997–8007. [PubMed: 24074025]

16. Rishton GM. Nonleadlikeness and leadlikeness in biochemical screening. Drug Discov Today. 2003; 8(2):86–96. [PubMed: 12565011]

17. Vickers CJ, Olsen CA, Leman LJ, Ghadiri MR. Discovery of HDAC Inhibitors That Lack an Active Site Zn2+-Binding Functional Group. ACS Med Chem Lett. 2012; 3(6):505–508. [PubMed: 24900500]

18. Chen Y, Cohen SM. Investigating the Selectivity of Metalloenzyme Inhibitors in the Presence of Competing Metalloproteins. Chem Med Chem. 2015; 10(10):1733–1738. [PubMed: 26412596]

19. Bruhn KW, Spellberg B. Transferrin-mediated iron sequestration as a novel therapy for bacterial and fungal infections. Curr Opin Microbiol. 2015; 27:57–61. [PubMed: 26261881]

20. Vinkenborg JL, Koay MS, Merkx M. Fluorescent imaging of transition metal homeostasis using genetically encoded sensors. Curr Opin Chem Biol. 2010; 14(2):231–237. [PubMed: 20036601]

21. Que EL, et al. Quantitative mapping of zinc fluxes in the mammalian egg reveals the origin of fertilization-induced zinc sparks. Nat Chem. 2015; 7(2):130–139. [PubMed: 25615666]

22. Fahrni CJ. Biological applications of X-ray fluorescence microscopy: exploring the subcellular topography and speciation of transition metals. Curr Opin Chem Biol. 2007; 11(2):121–127. [PubMed: 17353139]

23. Qin Z, Caruso JA, Lai B, Matusch A, Becker JS. Trace metal imaging with high spatial resolution: Applications in biomedicine. Metallomics. 2011; 3(1):28–37. [PubMed: 21140012]

24. McRae R, Bagchi P, Sumalekshmy S, Fahrni CJ. In Situ Imaging of Metals in Cells and Tissues. Chem Rev. 2009; 109(10):4780–4827. [PubMed: 19772288]

25. Carmona A, Roudeau S, Perrin L, Veronesi G, Ortega R. Environmental manganese compounds accumulate as Mn(ii) within the Golgi apparatus of dopamine cells: relationship between speciation, subcellular distribution, and cytotoxicity. Metallomics. 2014; 6(4):822–832. [PubMed: 24549144]

26. McRae, R. Investigating metal homestasis in mammalian cells using high resolution imaging techniques. 2010. (https://smartech.gatech.edu/handle/1853/41197)

27. Yang L, et al. Imaging of the intracellular topography of copper with a fluorescent sensor and by synchrotron x-ray fluorescence microscopy. Proc Natl Acad Sci USA. 2005; 102(32):11179–11184. [PubMed: 16061820]

28. Namdar M, et al. Selective inhibition of histone deacetylase 6 (HDAC6) induces DNA damage and sensitizes transformed cells to anticancer agents. Proc Natl Acad Sci USA. 2010; 107(46):20003–20008. [PubMed: 21037108]

29. Twining BS, et al. Quantifying Trace Elements in Individual Aquatic Protist Cells with a Synchrotron X-ray Fluorescence Microprobe. Anal Chem. 2003; 75(15):3806–3816. [PubMed: 14572047]

30. Hall MD, et al. The fate of platinum(II) and platinum(IV) anti-cancer agents in cancer cells and tumours. J Struct Biol. 2006; 155(1):38–44. [PubMed: 16630726]

31. Brady MJ, Bourbonais FJ, Saltiel AR. The Activation of Glycogen Synthase by Insulin Switches from Kinase Inhibition to Phosphatase Activation during Adipogenesis in 3T3-L1 Cells. J Biol Chem. 1998; 273(23):14063–14066. [PubMed: 9603900]

32. Samuni Y, Flores-Santana W, Krishna MC, Mitchell JB, Wink DA. The inhibitors of histone deacetylase suberoylanilide hydroxamate and trichostatin A release nitric oxide upon oxidation. Free Radical Biol Med. 2009; 47(4):419–423. [PubMed: 19447172]

33. Richon VM, et al. Second generation hybrid polar compounds are potent inducers of transformed cell differentiation. Proc Natl Acad Sci USA. 1996; 93(12):5705–5708. [PubMed: 8650156]

34. Lauffer BEL, et al. Histone deacetylase (HDAC) inhibitor kinetic rate constants correlate with cellular histone acetylation but not transcription and cell viability. J Biol Chem. 2013; 288:26926–26943. [PubMed: 23897821]

35. Hess-Stumpp H. Histone deacetylase inhibitors and cancer: from cell biology to the clinic. Eur J Cell Biol. 2005; 84(2–3):109–121. [PubMed: 15819394]

36. Lobera M, et al. Selective class IIa histone deacetylase inhibition via a nonchelating zinc-binding group. Nat Chem Biol. 2013; 9(5):319–325. [PubMed: 23524983]

37. Shirahama K, Yazaki Y, Sakano K, Wada Y, Ohsumi Y. Vacuolar Function in the Phosphate Homeostasis of the Yeast Saccharomyces cerevisiae. Plant Cell Physiol. 1996; 37(8):1090–1093. [PubMed: 9032964]

38. Vogt S. MAPS: A set of software tools for analysis and visualization of 3D X-ray fluorescence data sets. J Phys IV France. 2003; 104:4.

39. Shi P, et al. Synapse microarray identification of small molecules that enhance synaptogenesis. Nat Commun. 2011; 2:510. [PubMed: 22027590]

40. Zor T, Selinger Z. Linearization of the Bradford Protein Assay Increases Its Sensitivity: Theoretical and Experimental Studies. Anal Chem. 1996; 236(2):302–308.
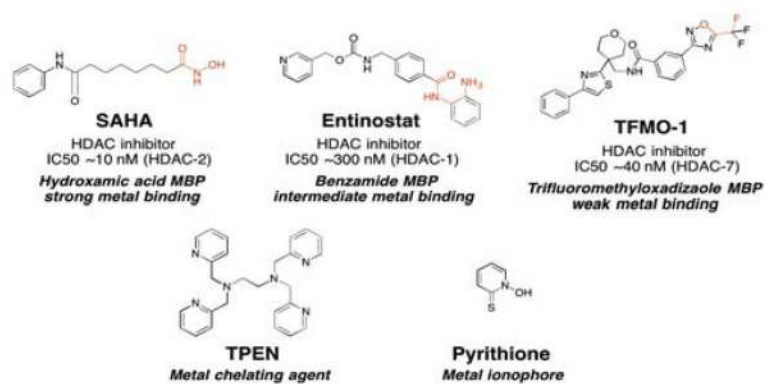
Fig. 1.
HDACi with different metal-binding ability (MBPs highlighted in red) and a control compound (TPEN) used for comparative studies. IC$_{50}$ xvalues are listed for the HDAC isoform for which each inhibitor is most active.
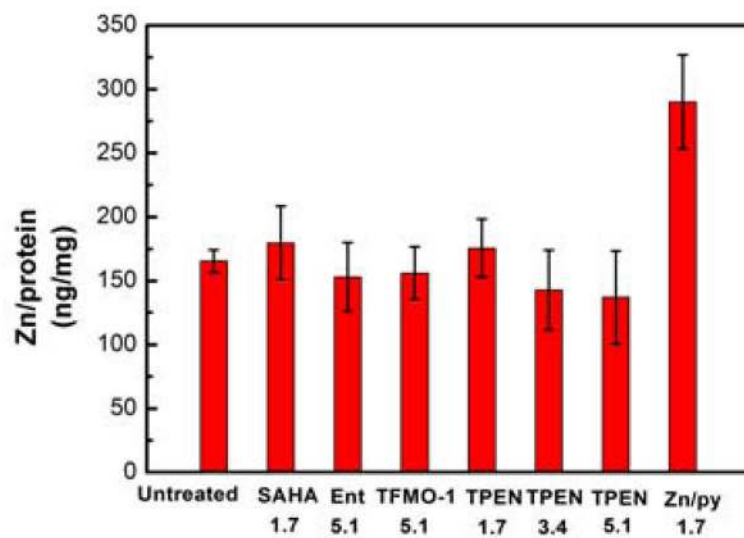
Fig. 2.
Overall Zn content in treated and untreated cells. Samples from left to right: untreated cells, 1.7 μM SAHA, 5.1 μM entinostat, 5.1 μM TFMO-1, 1.7 μM TPEN, 3.4 μM TPEN, 5.1 μM TPEN and 1.7 μM $ZnCl_2$/0.28 μM pyrithione treated cells. The cells were treated for ~2 h.
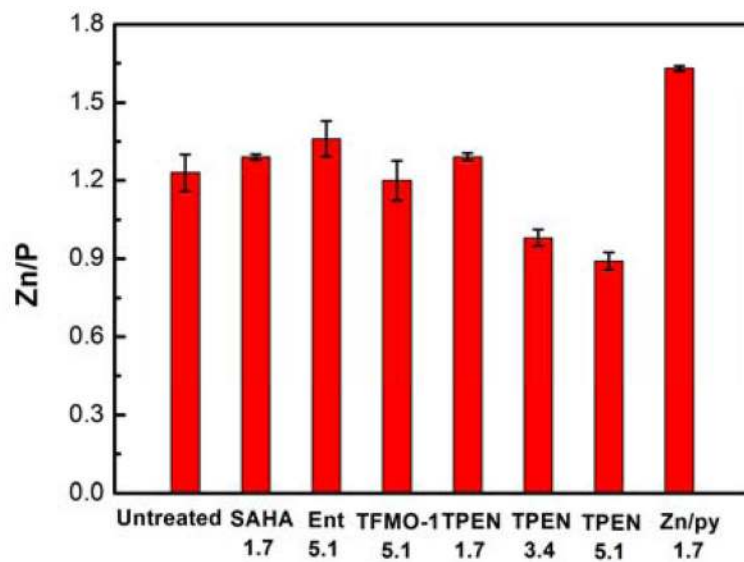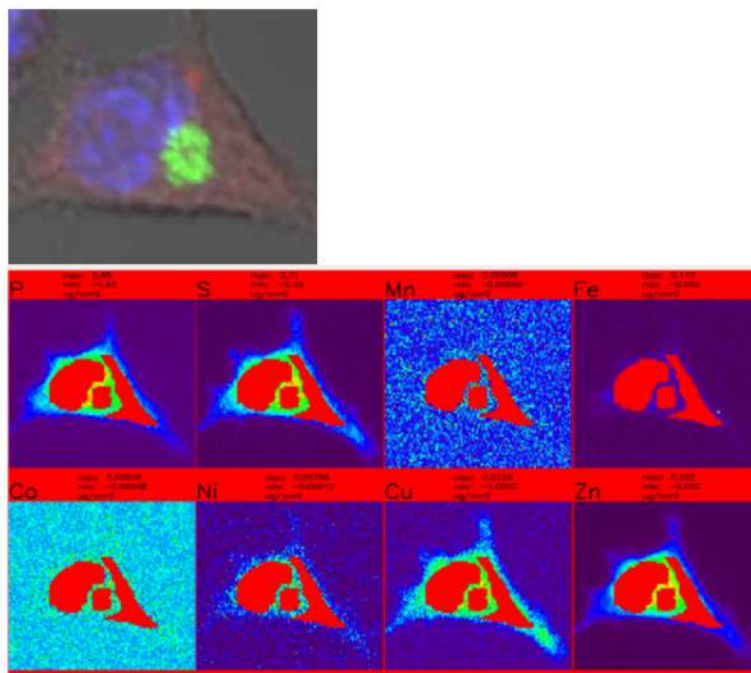
Fig. 3.
Relative cellular Zn/P content in treated and untreated cells. From left to right: untreated cells, 1.7 μM SAHA, 5.1 μM entinostat, 5.1 μM TFMO-1, 1.7 μM TPEN, 3.4 μM TPEN, 5.1 μM TPEN and 1.7 μM $ZnCl_2$/0.28 μM pyrithione treated cells. The cells were treated for ~2 h.

Fig. 4.
Top: Representative NIH3T3 cell confocal image. The Golgi body (green) was stained using CellLight GFP BacMam 2.0; the mitochondria (red) was stained by MitoTracker® Red CMXRos; and the nucleus (blue) was stained by Hoechst 33342. *Bottom*: The confocal image was overlaid with the SXRF elemental mapping, and MAPS software was used to analyze the elemental distribution in different regions of interest (the Golgi body, mitochondria, and nucleus are marked in red, and each organelle was analyzed separately).
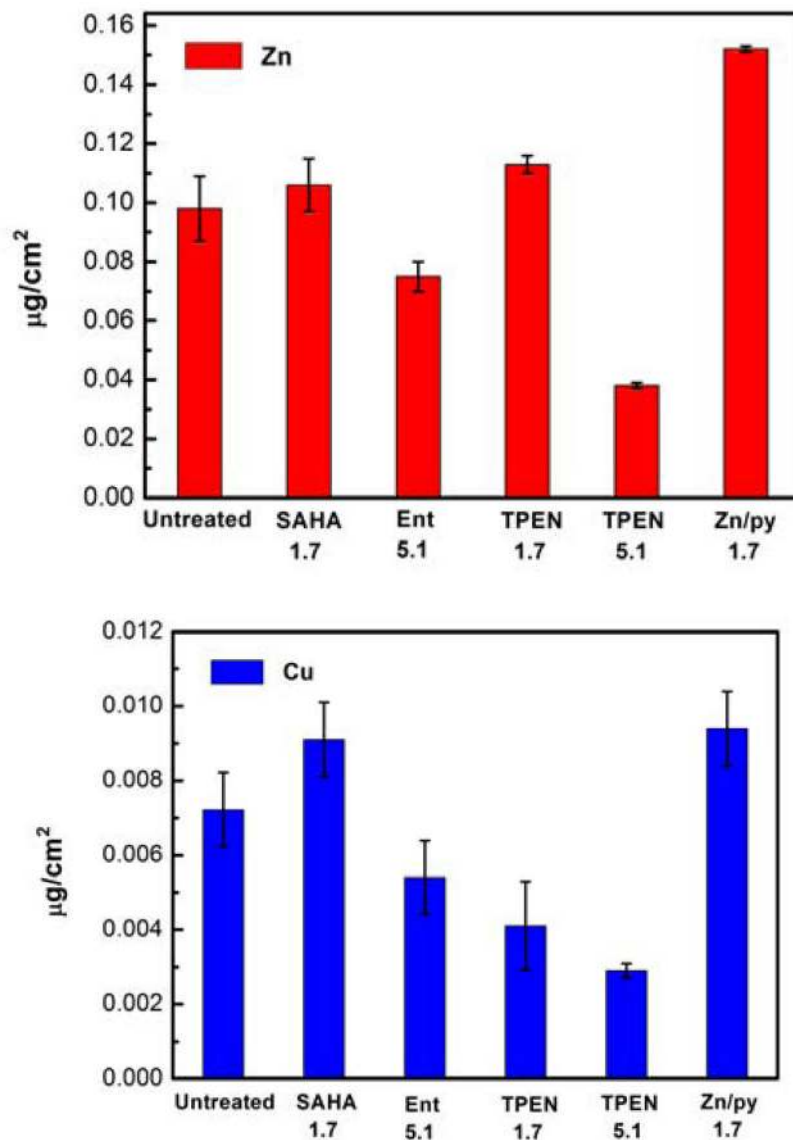
Fig. 5.

Top: SXRF results for the cellular Zn content in different samples. *Bottom*: SXRF results for the cellular Cu content in different samples. Samples from left to right: untreated cells, 1.7 μM SAHA, 5.1 μM entinostat, 1.7 μM TPEN, 5.1 μM TPEN and 1.7 μM $ZnCl_2$/0.28 μM pyrithione treated cells. The cells were treated for ~2 h.
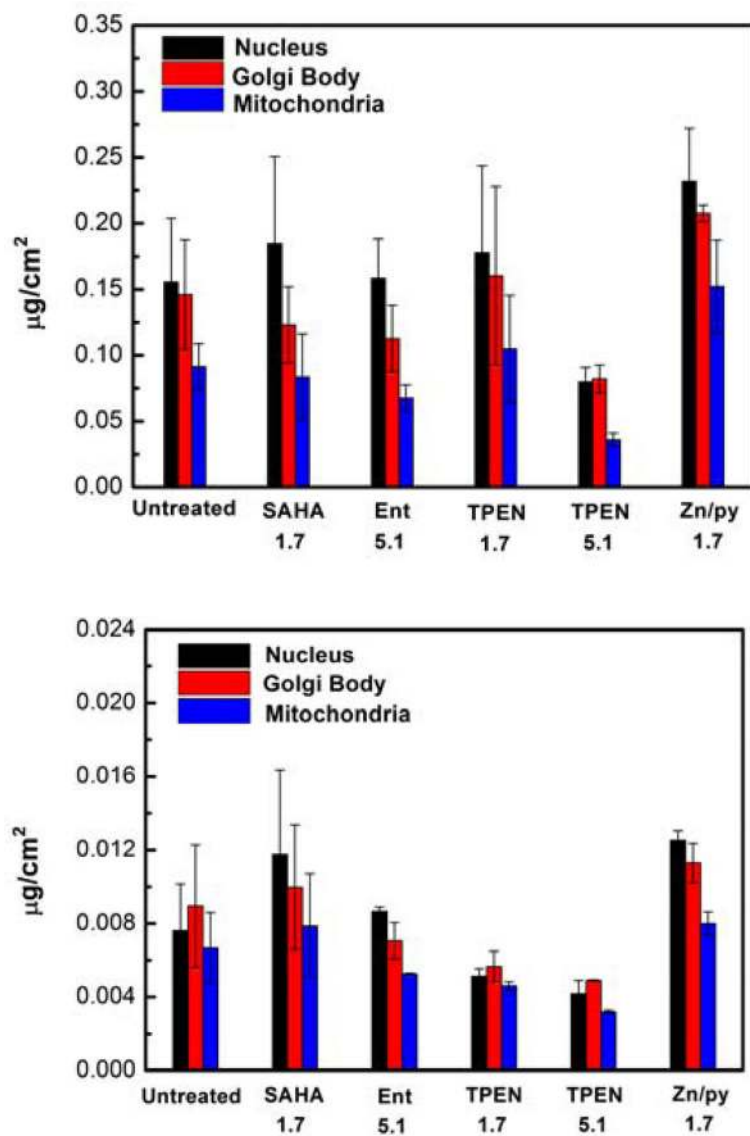
Fig. 6.

Top: Zn content in nucleus (black), Golgi body (red) and mitochondria (blue) in different samples. *Bottom*: Cu content in nucleus (black), Golgi body (red) and mitochondria (blue) in different samples. Samples from left to right: untreated cells, 1.7 μM SAHA, 5.1 μM entinostat, 1.7 μM TPEN, 5.1 μM TPEN and 1.7 μM Zn/0.28 μM pyrithione treated cells. The cells were treated for ~2 h.

Table 1

EC_{50} values of compounds against NIH3T3 cells, and the sub-lethal concentrations of compounds used in this study (all EC_{50} values are based on three independent trials).

	SAHA	Entinostat	TFMO-1	TPEN	ZnCl$_2$/pyrithione
EC$_{50}$ (μM)	4.8± 1.0	40.7 ± 3.8	75.3±5.4	25.7± 1.2	N/A
Conc. (μM)	1.7	5.1	5.1	1.7, 3.4,5.1	1.7/0.28